PCCP

Accepted Manuscript

ROYAL SOCIETY OF CHEMISTRY

www.rsc.org/pccp

An aqueous method for the controlled manganese (Mn^{2+}) substitution in superparamagnetic iron oxide nanoparticle for contrast enhancement in MRI

Ansar Ereath Beeran[a1], Shaiju. S. Nazeer[b1], Francis Boniface Fernandez[c1], Krishna Surendra Muvvala[2], Wilfried Wunderlich[3], Sukumaran Anil[d4], Sajith Vellappally[e4], Ramachandra Rao M.S.[2], Annie John[c1], Ramapurath. S. Jayasree[b1], Harikrishna Varma P R[a1*].

[a] Bioceramics Laboratory, [b] Biophotonics and Imaging Lab, [c] Transmission Electron Microscopy Laboratory,

[1] Biomedical Technology Wing, Sree Chitra Tirunal Institute for Medical Sciences & Technology, Poojappura

[2] Department of Physics, Indian Institute of Technology Madras, Chennai

[3]Department of Materials Science, Faculty of Engineering, Tokai University, Kitakaname 4-1-1, Hiratsuka-shi, Japan

[d] Division of Periodontics, College of Dentistry, [e] Dental Health Department, College of Applied Medical Sciences

[4] King Saud University, Riyadh, Saudi Arabia.

* Author for Correspondence: e-mail: varma@sctimst.ac.in

Abstract

Despite the success in the use of superparamagnetic iron oxide nanoparticles (SPION) for various scientific applications, its potential in biomedical field has not been exploited to the best. In this context, an in-situ substitution of Mn^{2+} was performed in SPION and a series of ferrite particles, $Mn_xFe_{1-x}Fe_2O_4$ with varying molar ratio of Mn^{2+}: Fe^{2+} where 'x' varies from 0-0.75. The ferrite particles thus obtained were further studied for MRI contrast applications and showed appreciable enhancement in the MRI contrast properties. Manganese substituted ferrite nanocrystals (MnIOs) were synthesized through a novel one-step aqueous co-precipitation method based on the use of combination of sodium hydroxide and trisodium citrate (TSC). This approach yielded the formation of highly crystalline, superparamagnetic MnIOs with good control over their size and bivalent Mn ion crystal substitution. Presence of TSC hydrophilic layer on the surface facilitated easy dispersion of the materials in an aqueous media. The primary characterizations such as structural, chemical and magnetic

properties demonstrated successful formation of manganese substituted ferrite. More significantly, MRI relaxivity of MnIOs improved fourfold than SPION crystals imparting high potential to use it as MRI contrast agent. Further, the cytocompatibility and blood compatibility evaluations demonstrated excellent cell morphological integrity even at higher concentrations of nanoparticles supporting the non toxic nature of nanoparticles. These results open new horizons for the design of biocompatible water dispersible ferrite nanoparticles with good relaxivity property *via* a versatile and easily scalable co-precipitation route.

Introduction

The superparamgnetic iron oxide (SPION) nanoparticles and their dispersions have great interest in the area of modern materials science,[1,2] especially biomedical science. Due to their outstanding property, superparamagnetic crystals having nanometer size and high saturation magnetization are emerging as powerful candidates for biomedical applications like drug delivery,[3,4] cancer hyperthermia,[5] biosensors,[6,7] and bioimaging.[8] However, the common spinel ferrite iron oxides have intrinsic magnetic properties with standards far below that of optimal requirement for diverse biomedical applications. In order to improve their efficiency for various applications, the spinal ferrite nanoparticles with particular physical and magnetic properties are modified during the synthesis process.[9-11]

One among the best technique for magnetic modification is crystal ion substitution with appropriate candidates, which can provide a versatile strategy to tune the SPION crystal structure.[12] It is known that the SPION crystals exist as cubic spinel structure, with the oxygen atoms forming an fcc close packing and Fe^{2+}, Fe^{3+} occupying tetrahedral or octahedral interstitial sites and is generally represented as MFe_2O_4.[13,14] By altering the chemical identity of M^{2+}, the magnetic property of MFe_2O_4 can be increased considerably.[15]

There are several d block elements such as Mn, Co, Ni, Cu and Zn which when incorporated to crystal structure of SPIONs favors spinel crystal formation resulting in enhanced magnetic property and relaxivity compared with bare SPIONs which is more suited for applications like MRI.[16,17] Spinel structures developed through doping of SPIONs with Ni^{2+} and Cu^{2+} are sensitive to leaching and can cause cytotoxicity. Hence these systems require further treatment for stability, while doping of Zn^{2+} to SPIONs produces hydrophobic nanoparticle with superior magnetic moment and negative contrast effect.[18] The major drawback of this system is its high solubility in acidic and basic pH conditions. It is noteworthy to mention that Co^{2+} doping with SPIONs is not preferred due to the non-superparamagnetic nature of the resultant crystal structure and high toxicity of Co ions.[19,20] However, manganese ion (Mn^{2+}) doped SPION crystals possess highest magnetization value compared to other doping agents reported so far. Moreover, these Mn^{2+} doped SPION crystals also demonstrate higher transverse relaxivity values. [21-26]

Various methods have been evolved for the preparation of SPION crystal modification, including thermal decomposition,[27] co-precipitation,[28] microemulsion, hydrothermal and sonochemical process.[29,30] The most common protocols for the preparation are thermal decomposition and co-precipitation techniques. The former method can easily produce size controlled ferrite nanoparticle under higher temperature in organic medium.[15] But these particles are hydrophobic with hydrocarbon molecules at the periphery of surfactants and thus insoluble in aqueous media. To transform the nanoparticles into water dispersible, one requires different additional steps.[31] In this context, the current challenge is to develop a novel synthesis method for aqueous dispersed magnetic nanoparticle having enhanced magnetic property and biocompatibility.

Aqueous based co-precipitation method represents a simple and versatile tool to prepare nanocrystals not readily accomplishable by other methods. It is cost effective,

provides high yield, less time consuming and easily scalable to large scale production. In addition to these advantages, it is an eco-friendly route because there is no use of hazardous solvent, chemicals and high temperature or pressure.[32,33]

In this study, we are presenting a novel synthesis method to prepare Mn^{2+} substituted SPION crystals (MnIO) through the ideal aqueous co-precipitation route. The various compositions of Mn^{2+} doped MnIO systems were synthesized by a one-step co-precipitation route incorporating base induced precipitation. A low concentration of trisodium citrate (TSC) salt was used during the synthesis. The Manganese substitutions in the SPION crystals were performed with different molar concentrations of Mn^{2+} and a composition of $Mn_xFe_{1-x}Fe_2O_4$ with varying molar ratio of Mn^{2+}: Fe^{2+} were developed where 'x' varies from 0-0.75. A thorough evaluation of synthesized nanocrystals was carried out based on the morphology, structure, chemical composition, magnetic properties and biocompatibility. The synthesized nanocrystals possess excellent transverse relaxivity and good biocompatibility properties and can be used as effective MRI contrast agents. This study throws new light on the fabrication of novel superparamagnetic MRI contrast agent through a low cost and environmental friendly co-precipitation method.

2. Results and discussions

The co-precipitation synthesis route has enabled in-situ formation of bivalent Mn substituted superparamagnetic nanoparticle as colloidal suspension and is schematically represented in Fig. 1. In an earlier study, cation - substituted superparamagnetic nanocrystals were synthesized by co precipitation in a high temperature organic media.[34] However, the present study focused on the easiest aqueous co-precipitation route for making nanoparticles with maximum concentration of Mn^{2+} substitution in the SPION crystals. SPION nanocrystal formation is highly sensitive to the percentage substitution of foreign ions since excess

amount of bivalent oxidation state ion (Mn^{2+}) do not favour the spinel crystal formation. Therefore, with this regard, we have further extended the study to optimize the maximum feasible quantity of Mn^{2+} incorporation to the SPION crystals using this aqueous synthesis route. The maximum substitution of Mn^{2+} in the SPION was optimized to 75% molar concentration of ferrous ions (3:1 Mn^{2+}: Fe^{2+}); beyond which manganese ion could not form superparamagnetic nanocrystals.

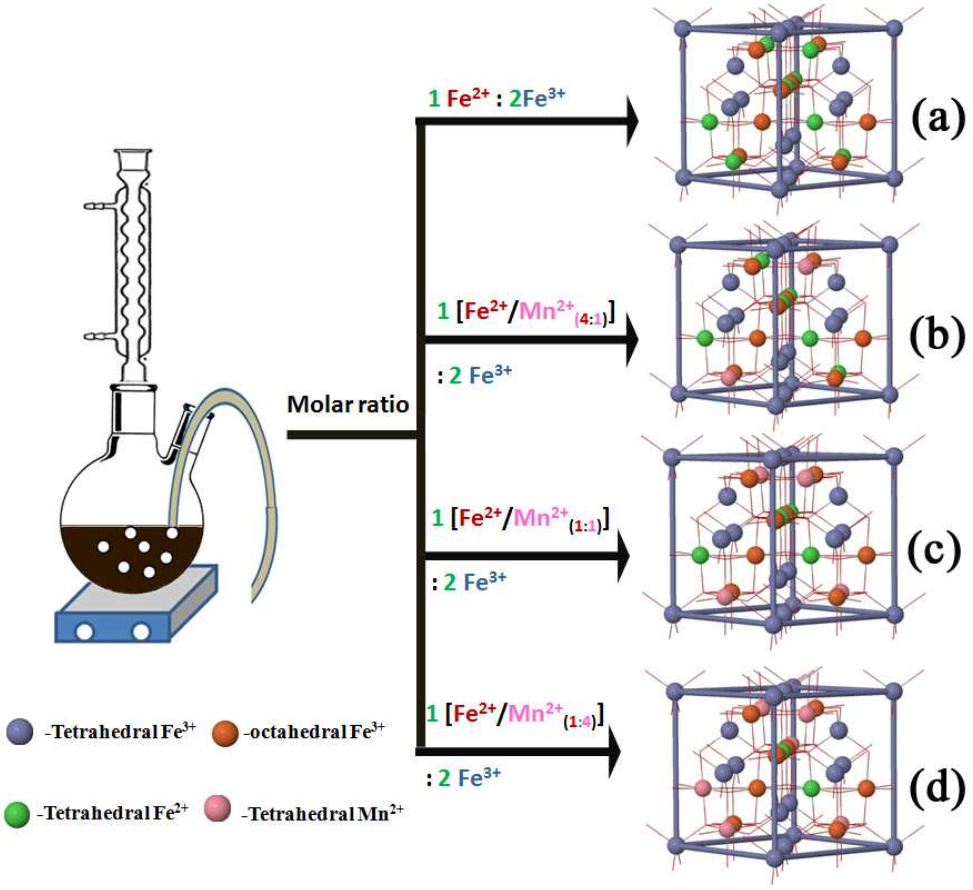

Fig. 1 Proposed Schematic representation of Mn^{2+} substituted SPION crystals. (a) SPION (b) MnIO25 (c) MnIO50 (d) MnIO75.

The SPION have an inverse spinel crystal and its cation distributions are $Fe^{+3}{}_A$ $[Fe^{+3}Fe^{+2}]_B$ O_4, where A and B are tetrahedral and octahedral sites respectively. This must be

due to the smaller size and favorable orbital splitting energy of Fe^{3+} ion occupied in the tetrahedral and the octahedral interstitial sites proportional to the Fe^{3+} and Fe^{2+} ions. The incorporation of bivalent manganese ion has changed the occupancy of inverse spinel arrangement of cations in Fe_3O_4 crystals and has favored the formation of mixed spinel structure in ferrite crystals. In the MnIOs, the spinel with a cubic oxygen lattice of cations distribution was formed with expected chemical formula $(Mn^{2+}_{1-c}\ Fe^{3+})_A[Mn^{2+}_cFe^{3+}_{2-c}]_BO_4$.

The precipitation of nanocrystals was carried out in the presence of trisodium citrate solution. This has favored the homogeneous nanoparticle formation of manganese ferrite crystals. The absence of citrate ions caused formation of large clumps of manganese ferrites posing significant difficulty in dispersing these particles in water, hindering their use as contrast agents.[35,36] Moreover in the magnetic nanocrystal formation, after the nucleation step, van der Waals and electrostatic forces govern the formation of clusters. In the presence of TSC, nanoparticles gain negative surface potential which could overcome these attractive forces. Here the Mn^{2+} has maximum number of unpaired electrons and similar size to iron atom, and has favoured the isomorphous substitution of ferrous cation by manganese in the co-precipitation route. By this argument, we can make the ferrite with very high substitution efficiency (75% molar concentration of the ferrous ion) for achieving high quality superpramagnetic nanostructure formation. Indeed the typical syntheses of MnIOs were carried out to produce large quantity of nanoparticles in a one-pot reaction without sacrificing the characteristics of superparamagnetic nanoparticles.

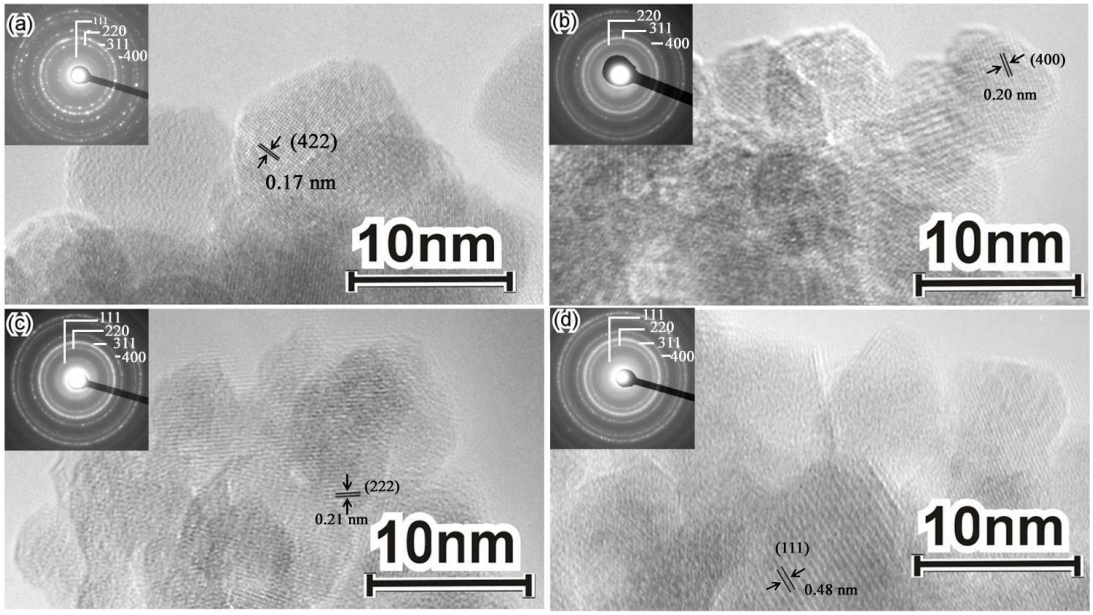

Fig. 2 HRTEM images of various molar concentrations of Mn^{2+} substituted iron oxide crystals. a) SPION b) MnIO25 c) MnIO50 d) MnIO75.

The HRTEM images show the size and shape of the MnIOs and are depicted in Fig. 2. The HRTEM and its FFT investigation indicate that nearly all of the nanoparticles form single crystals of ferrite containing highly crystalline structure. A careful inspection of the HRTEM image further revealed the presence of some crystal defect in few particles. However, the d spacing measurements from HRTEM and the corresponding FFT generations are in good agreement with interplanar distances derived from XRD studies

The above MnIOs demonstrate smaller size than those prepared by co-precipitation through NH_3, TMAOH etc. of previous reports.[37-39] Moreover, similar type of size changes were observed with various molar percentages of Mn^{2+} substitution in SPION and increasing particle size was in the order: MnIO25 ≈ MnIO50 < MnIO75 < SPION. This probably could have resulted with the progressive increase in the solubility constant of corresponding divalent metal hydroxides.

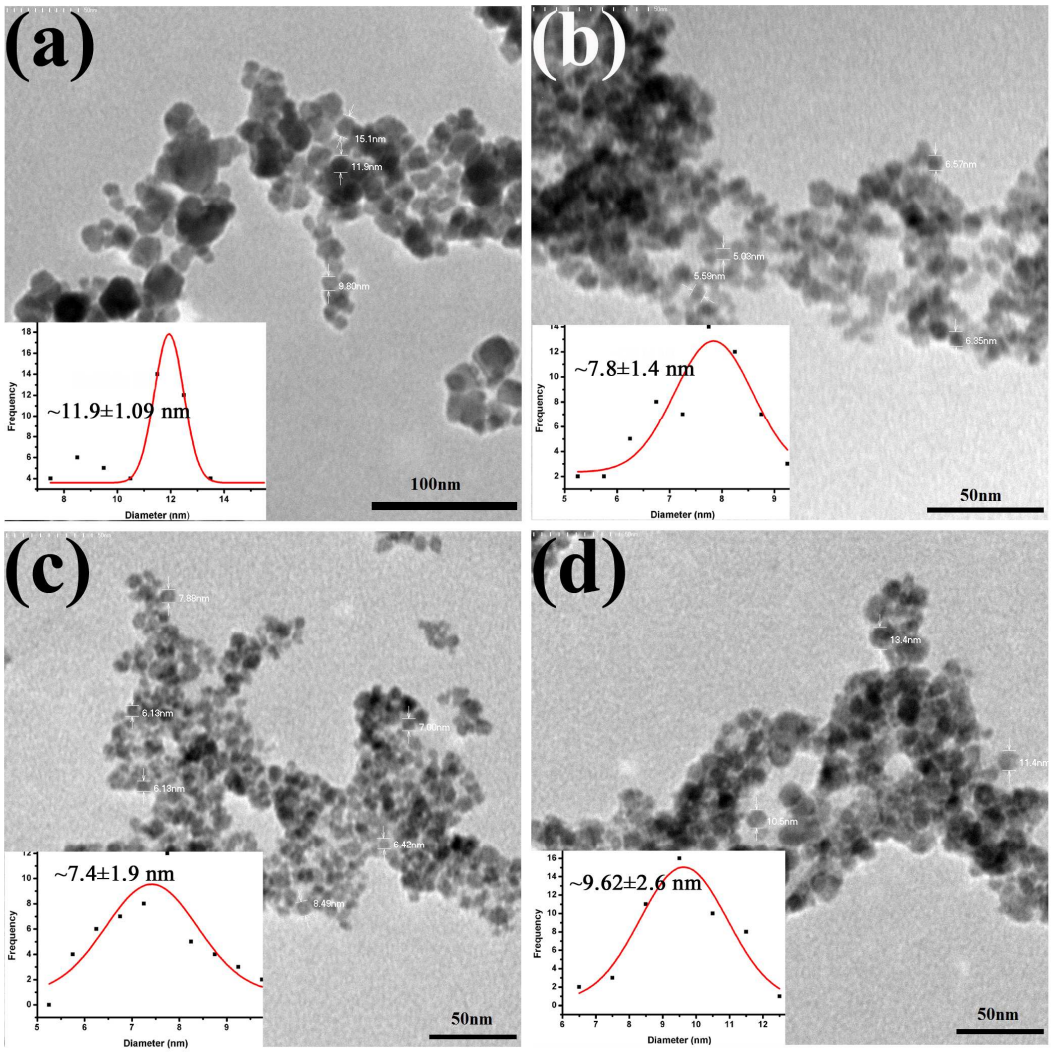

Fig. 3 TEM images and corresponding size distribution curve shows in inset a) SPION b) MnIO25 c) MnIO50 d) MnIO75.

The TEM images as depicted in Fig.3 demonstrates that the samples consist of polygonal faceted spherical nanoparticles and have narrow size distribution with average values of ~11.9±1.09 nm for SPION, ~7.8±1.4 nm for MnIO25, ~7.4±1.9 nm for MnIO50, and ~9.62±2.6nm for MnIO75. This is in good agreement with the calculated values of crystallite sizes from the X-ray diffraction technique. Also the selected area diffraction patterns are very similar for all the samples, comparable to spinel ferrite and reveals that these nanoparticles are highly crystalline.

XRD analysis was performed to identify the crystallographic structure and to estimate the crystallite size (Fig.4). The molar concentrations of Mn^{2+} 25%, 50% and 75% of ferrous ion in the compositions of MnIOs matches with (PDF= 01-071-6336) SPION diffraction pattern, the positions and relative intensities of the strong peaks confirming the Bragg reflections indexed inverse cubic spinel structure (Fd3m). Each sample contains identical peaks regardless of bivalent Mn content, and there are no peaks corresponding to MnO_2 or Mn_3O_4, confirming that the bivalent Mn is incorporated into the ferrite structure rather than precipitating as a manganese oxide or hydroxide along with the SPION. This could be attributed to the similarity of ionic charge and radii of Fe^{2+} and Mn^{2+}. However, the scenario changes when the Mn^{2+} concentration is more than 75% molar concentration of ferrous ions.

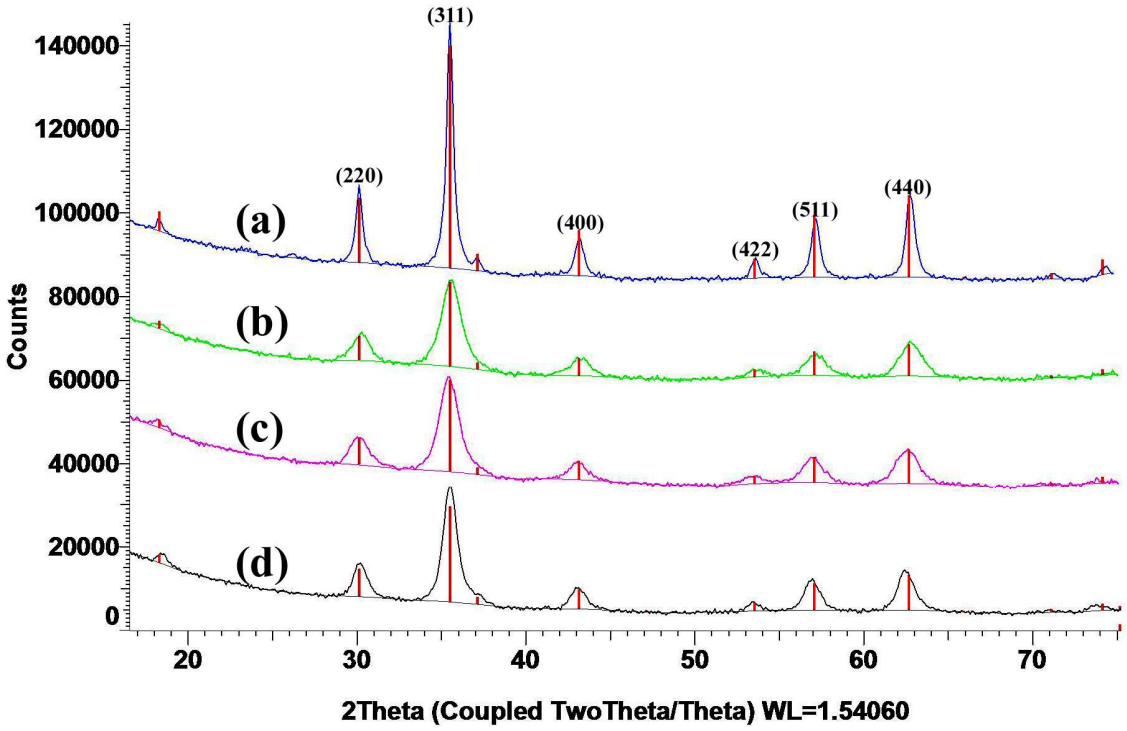

Fig. 4 X-ray diffraction pattern of a) SPION b) MnIO25 c) MnIO50 d) MnIO75 nanoparticle assemblies.

The XRD patterns of MnIOs presented in the Fig.4, support that no phases other than nanocrystalline manganese ferrite are present up to critical concentration. On the other hand, beyond the critical molar concentration (75% of ferrous ion) of Mn^{2+}, the final system did not support the crystal formation where the major peaks of spinel disappears (ESI, † Fig. S1). The average crystal size of nanoparticles range from ~11.5±0.8nm for SPION, ~8.6± 0.9 nm for MnIO25, ~8.1± 0.6nm for MnIO50 and ~9.7±0.9 nm for MnIO75 and the crystal size of the nanoparticles calculated by Scherrer formula using (311) peak matches with size calculated by TEM analysis. Moreover, the peak broadening is in good agreement with the variation in particle size detected by TEM. The results revealed that trisodium salt with NaOH plays an additional role in controlling the particle size besides acting as a co-precipitation agent. However, these molecules did not induce any complex formation other than magnetic phase of the nanocrystals.

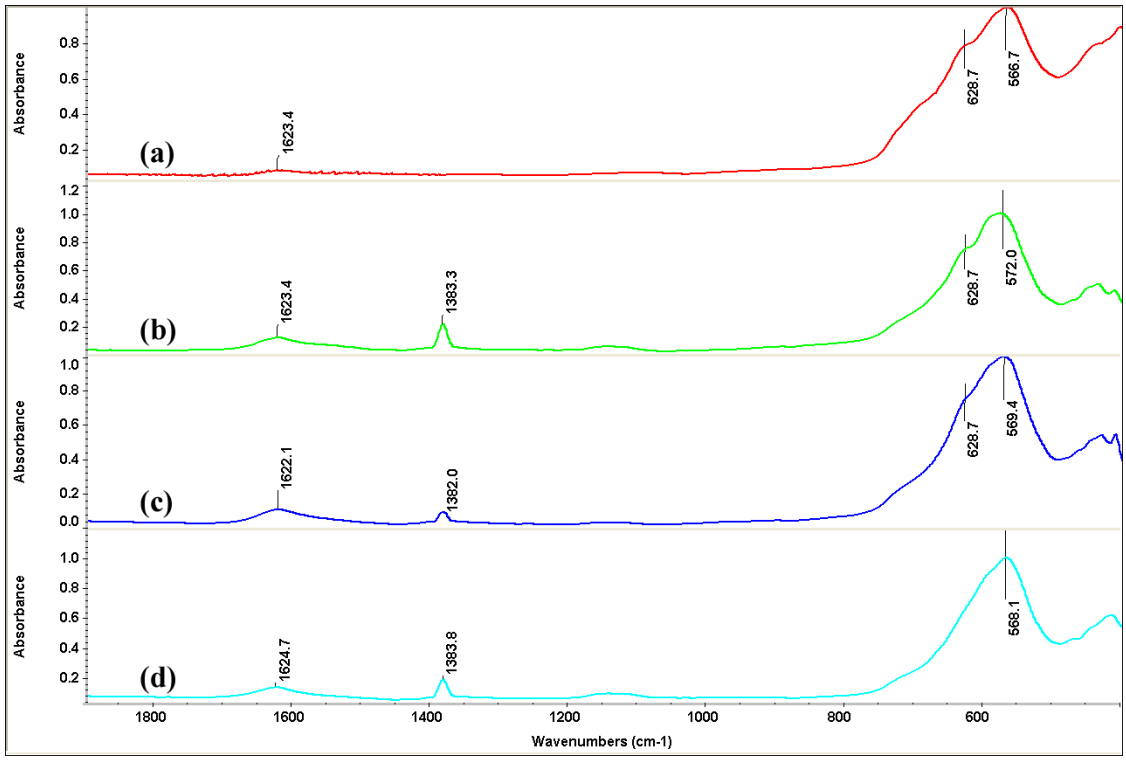

Fig. 5 FTIR spectra of a) SPION b) MnIO25 c) MnIO50 d) MnIO75 nanoparticles in the 1900-400 cm^{-1} range.

The FTIR spectra of (a) SPION, (b) MnIO25 (c) MnIO50 and (d) MnIO75 in the range of 1900-400 cm^{-1} are depicted in Fig. 5. Generally, iron oxide and manganese ferrite shows M_T-O-M_O stretching band at ~600-500 cm^{-1}, where M_T and M_O correspond to the tetrahedral and octahedral positions, respectively. The FTIR spectra of different ferrites exhibit an intense peak at 575-550 cm^{-1}, corresponding to the characteristic peak of Fe-O stretching in iron oxide and Fe-O or Mn-O stretching of manganese ferrite. In addition to this intense peak, an additional weak shoulder peak at ~628 cm^{-1} that appears in nanoparticles also shows the presence of magnetite phase of nanocrystals.[40,41] The Fe-O vibration band has widened and weakened with increased manganese concentration and slightly shifted towards the lower wave number region. Moreover, there is no oxyhydroxide peak of Fe or Mn observed in the characteristic regions which further corroborates to the phase pure formation of Manganese ferrite.[42-44]

In ESI † Fig. S2, peaks at ~3395 and ~1595 cm^{-1} are characteristic bands of metal ferrites with O–H stretching and bending vibrations, respectively. In addition to the vibrational peaks of metal oxides, the MnIOs shows additional peaks at 1618 and 1397 cm^{-1} corresponding to the asymmetric and symmetric stretching of carboxyl group of citrate. Tri-sodium citrate also shows corresponding infrared bands at 1668 and 1390 cm^{-1}. The band at 1668 cm^{-1} of tri-sodium citrate, which corresponds to asymmetric stretching of carboxyl group, is shifted to 1618 cm^{-1} in the FTIR spectra of MnIOs. The shift in the peak position to a lower wave number region indicates the presence of strong hydrogen bonding which gives an indication of the strong binding of citrate on to the MnIOs surface.[45,46]

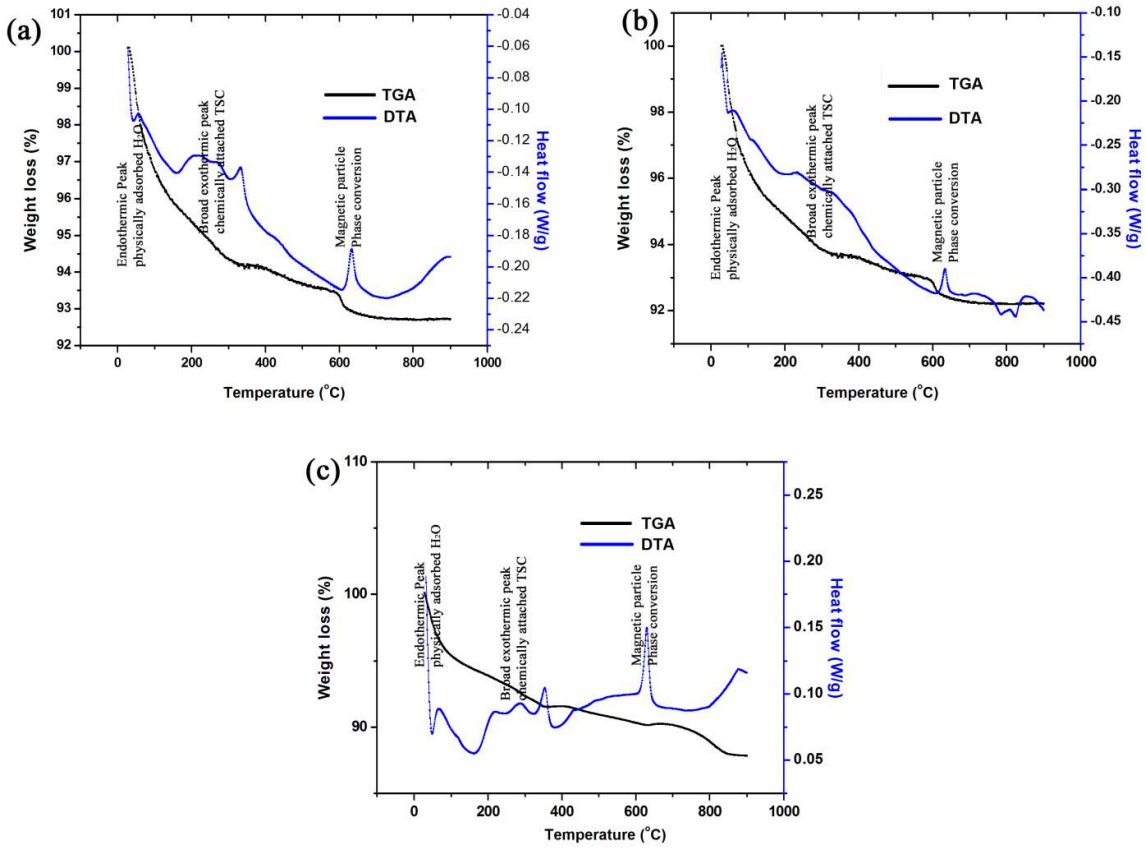

Fig. 6 TGA & DTA of a) MnIO25 b) MnIO50 c) MnIO75 nanoparticles under N_2 atmosphere.

The amount of trisodium citrate adsorbed on the nanomaterial surface was quantified by TGA-DTA and presented as Fig. 6. The TGA plot represents four distinct stages of thermal decompositions at temperatures, 143°C, 350°C, 605°C and 900°C. The total and partial weight losses are summarized in Table 1.

Temp (°C)	Weight % remaining		
	MnIO25	MnIO50	MnIO75
143	96.37	95.47	94.6
350	94.62	93.72	91.56
605	93.63	92.73	90.29
900	93.12	92.22	87.83

Table 1 Partial weight loss determined by TGA analysis

The TGA curves for all the bare samples display an initial weight loss of ~4-5wt% in the temperature range 30-143^{o}C are assigned to the removal of physically adsorbed water and hydroxyl groups from trisodium citrate, which shows endothermic peak. The following weight losses are due to decomposition of the citrate group adsorbed on the nanoparticle surfaces. The second major broad exothermic peak was observed between 143-350^{o}C showings a weight loss of ~1.5-3%. Weight loss in the second step indicates the dissociation of citrate–metal bond accompanied by the oxidative exothermic degradation of the citrate from the nanoparticle surface at higher temperature. The last stage of TGA-DTA resulted in the exothermic magnetic particle phase conversion region around 605^{o}C and due to loss of residual carbon.[47,48]

Different molar compositions of manganese ferrite nanocrystal Fe/Mn ratios were evaluated by EDX and ICP analysis. It is well known that EDX analysis gives the effective atomic concentration of different constituents on surface layer of the solid investigated. The energy dispersive X-ray analysis of prepared specimens was carried out at same voltage and at various areas on the surface of solid and is represented as Fe/Mn ratio in Fig. 7. Similarly, the relative atomic percentage of Mn, Fe and oxygen species present in the solid from theoretical calculation and ICP analysis are presented in Table 2.

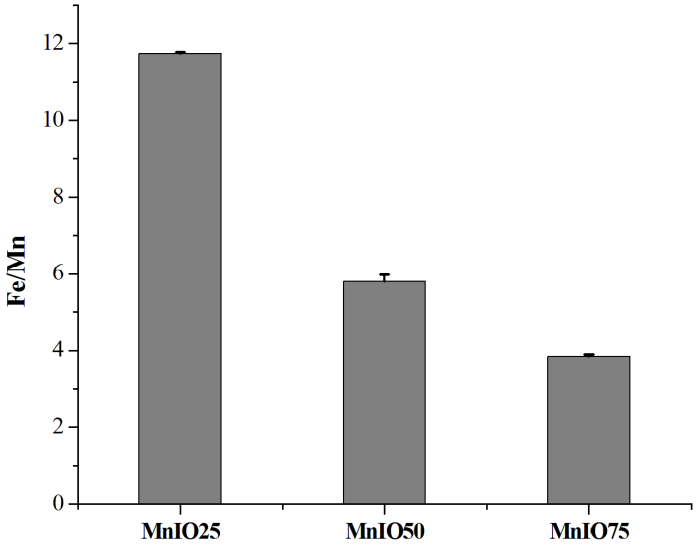

Fig. 7 Surface composition of Fe/Mn ratio of nanoparticle calculated via Energy dispersive spectrum.

	Theoretical	Fe/Mn (ICP)
MnIO25	11.18	11.60
MnIO50	5.08	5.43
MnIO75	3.05	3.28

Table 2 The initial Fe/ Mn metal composition ratio compared with ratios as determined by ICP-OES analysis.

The values indicate that the surface concentration of Mn atom increases with increase in the percentage of substitution in the SPION crystal. It gives a solid evidence for the effective incorporation of manganese ions in the spinel structure. Moreover the surface concentration of Mn, Fe and O atoms at 20keV on different areas over the surface of the specimen studied are much closer to each other. This finding supports the homogeneous composition of synthesized MnIOs. Table 2 shows the quantitative manganese content present in each of the

compositions of these magnetic nanocrystals confirmed by ICP analysis. The results indicate that the samples possess a slightly varied manganese content compared to stoichiometric manganese ferrite. But the Mn/Fe ratio is approximately equal to the EDX composition which confirms the phase pure substitution of manganese ion in the ferrite crystals.[49]

For enabling the biological applications, the synthesized MnIOs were tested for various recommended parameters. Haemocompatibility is of prime importance for nanoparticles used in imaging, as vasculature provides primary access and distribution in a living system. To ensure compatibility, haemolysis and clotting time evaluations were carried out (ESI,† Table S1). It is apparent that the nanoparticles concentrations up to 1mg per mL blood did not induce haemolysis. Maintenance of blood rheology is of prime importance in most intravenous interventions. Surface charged ferrites may induce aggregation during interaction with leukocytes and platelet cells.[50] MnIOs nanoparticles in a final concentration of 1 mg were used in the aggregation test. Particle aggregation was not observed in the case of RBC, WBC and platelets ESI,† Fig. S5, S6 & S7.

Alamar Blue assay was carried out to evaluate cellular activity in the presence of nanoparticles at varying concentration levels. HeLa cells were evaluated at 24 hours post – exposure to nanoparticles, data collected indicates more than 95% cellular activity across concentration levels used (ESI,† Fig. S3). Phase contrast images of cells in contact with nanomaterials also provide evidence on preservation of morphological characteristics of cells under the influence of nanoparticles. Comparison of cells from control wells to imagery of exposed cells indicates identical nature of cellular architecture even in higher doses of SPION and MnIOs concentration (ESI,† Fig. S4). Furthermore cellular uptake microscopic study of SPION and MnIOs in HeLa cells visualized by Prussian Blue staining shows the internalised particles of SPION and MnIOs (ESI,† Fig. S8).

One of the most important factors for nanoparticle based MRI contrast agent is its magnetic property and it depends on the crystal constitution by metallic cationic distribution among A and B sites of crystal constitution. The magnetic behavior of the MnIOs is expected to vary with different Mn^{2+} and Fe^{2+} positions in crystal structure because the Mn^{2+} ion is isotropic compared to other crystal atoms. The (M-H) loop of various composition of ferrite nanoparticles are shown in Fig. 8. It could be observed from the hysterysis loop that all composition of nanoparticles shows negligible remanence and coercivity, which confirms the superparamagnetic behavior of the nanoparticles. But, hysteresis curve of SPION shows minor remanence and coercivity as compared with the MnIOs, where they are nil (Inset of Fig.8). Recent studies report that manganese ferrite shows lower blocking temperature and higher magnetic saturation. This is because the Mn^{2+} cation in the spinel structure has five unpaired electron and all are in high spin state. Also the weak interaction of spin-orbital coupling gives small magnetic anisotropy energy barrier than SPION and it results the particles thermally activate to go through superparamagnetism via random flipping of its magnetization. Furthermore, the previous reports revealed that small MnIOs shows non-interacting property, which helps to the faster relaxation of particles. Hence the particle did not show any remanence and coercivity even at low field.[51,15] The values of saturation magnetization of pure SPION and MnIOs are represented in Table 3. Here the saturation magnetization of nanocrystals slightly varies for the Mn^{2+} substituted iron oxide crystals. The MnIO25 and MnIO50 of manganese substitution decreases the saturation magnetization as compared with bare iron oxide particles. However, further increase in Mn^{2+} to MnIO75 substitution (where the concentration of Fe^{2+} to Mn^{2+} is1:3), the saturation magnetization was found to be slightly improved. The shape of the hysteresis curve also is found to vary with the changes in Mn^{2+} substitution concentration.

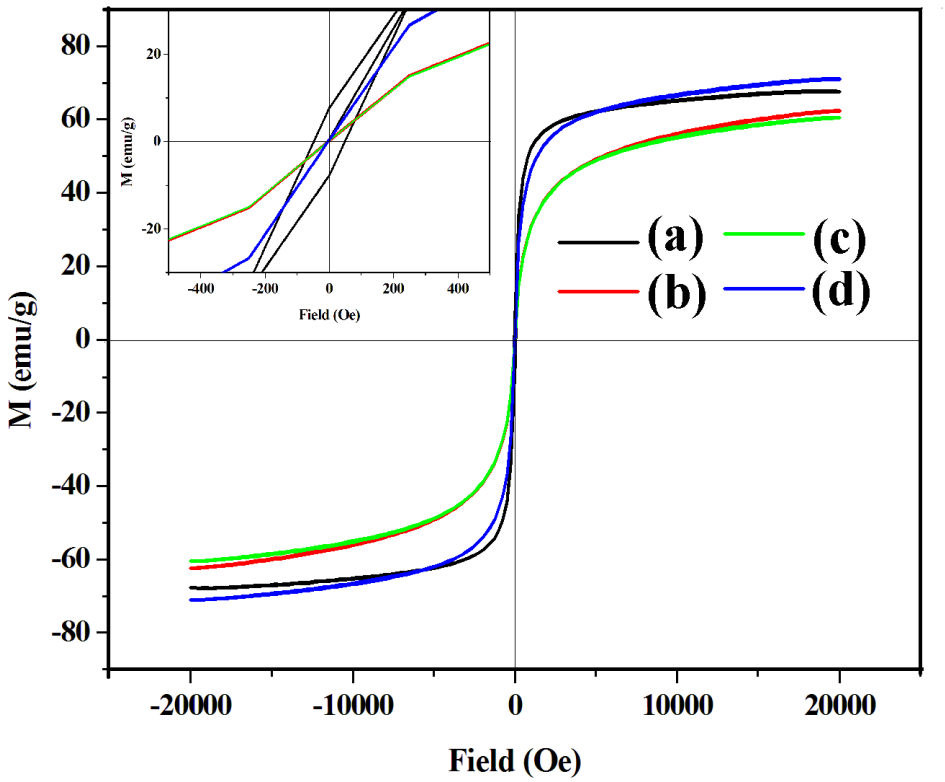

Fig. 8 Magnetic property measurement of MnIOs particles under room temperature a)SPION b)MnIO25 c)MnIO50 d)MnIO75 and its corresponding remanance and coercivity in the inset.

Sample	Magnetic saturation M(emu/g)	Relaxation (r_2) $mM^{-1}s^{-1}$
MnIO25	62.4	236.6
MnIO50	60.55	203.9
MnIO75	71.13	202.1
SPION	67.63	57

Table 3 Measurement of magnetic saturation and relaxivity values of MnIOs nanoparticles compared with SPION particles.

The bivalent manganese ion has five unpaired electrons in the outer shell and has higher magnetic moment as compared to the bivalent iron ion. Moreover, the MnIO25 and MnIO50

were found to be slightly small compared to the bare iron oxide crystals and therefore have more spin canting effect than SPION.[52] Furthermore, the observed results of the magnetization studies for the MnIO25 and MnIO50 were slightly distorted when compared to the slightly larger iron oxide particles resulting in lesser saturation magnetisation. This may be due to the smaller size and structural anisotropic nature of the particles. But in the case of MnIO75, the crystallite size is almost similar to SPION and it has demonstrated zero remanance and coercivity as compared with SPION. This can be clearly viewed from the intersection of loop with vertical magnetization axis in the inset of Fig. 8. In the case of magnetic materials, the coercivity field Hc for crystal refers to the intensity of magnetic field required to reduce the magnetization of the magnetic sample to zero. It has been observed from the magnetic measurement that, both Ms and Hc values decrease with increase in concentration of bivalent Mn ion in the crystal. This indicates that the incorporation of Mn^{2+} ion in the SPION matrix greatly enhance the magnetic isotropy of the crystal. Therefore, in a simple model the spinel ferrite of oxygen packed, face centered cubic lattice, the tetrahedral (T_d) and octahedral (O_h) sites were occupied by magnetic ions. In the case of manganese ferrite, with mixed spinel structure, the majority of T_d sites is expected to be occupied by $Mn^{2+}{}_{1-x}Fe^{3+}x$ ($0 < x < 1$) and O_h sites by $Mn^{2+}{}_x\ Fe^{3+}{}_{2-x}$. When an external magnetic field was applied to this structure, the magnetic spins (Mn^{2+}/Fe^{3+}) in O_h has aligned parallel to the direction of the external magnetic field but those in T_d has aligned anti parallel[53]. Moreover, the maximum magnetic susceptibility was shown by manganese ferrite due to the higher magnetic spin of manganese (contribution approximately $5\mu_B$), so that the higher concentration of manganese substitution in iron oxide replaces more and more magnetization deciding Fe^{2+} ion from the crystal position and the crystal acquires higher magnetic saturation.

Various molar composition of Mn^{2+} modified magnetic MnIO nanoparticles were tested as the MRI contrast agent. Due to the large magnetic moment, nanoparticles can modulate the MR signal enhancement effects. The spin–spin relaxation time was measured using T_2weighted MR images of each sample at 1.5 T (Fig. 9).

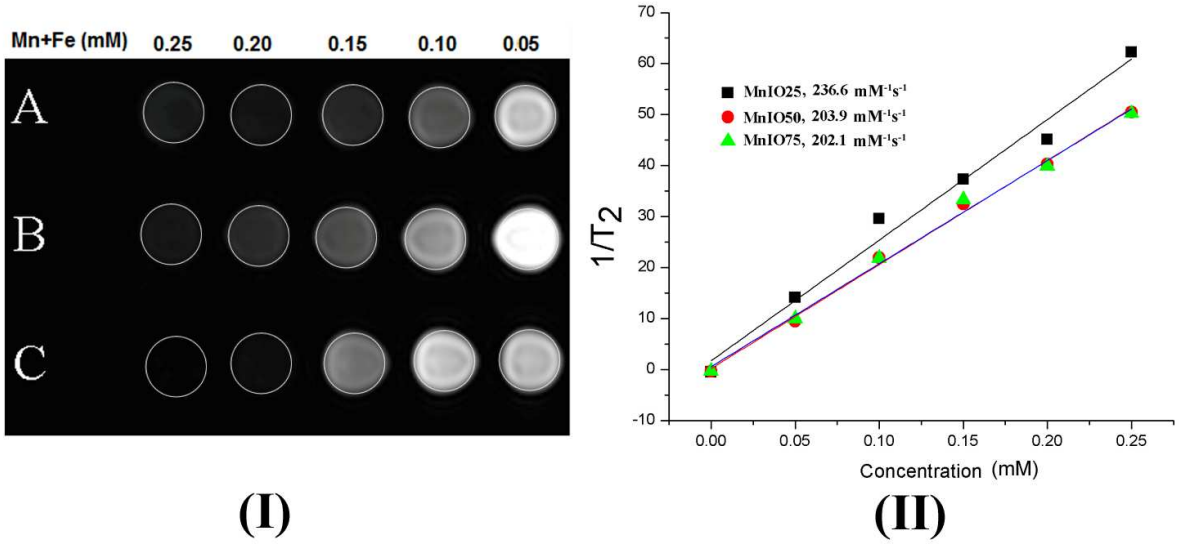

Fig. 9 (I) T_2weighted MR images of A) MnIO75 B) MnIO50 C) MnIO25 varying concentrations at 1.5T. (II) Relaxivity rate Graphs of $1/T_2$ against the Fe+Mn concentrations of MnIOs.

The magnetic relaxivities were calculated from the pixel intensity maps of different concentrations of SPION, MnIO25, MnIO50 and MnIO75. This corresponds to 57$mM^{-1}s^{-1}$, 236.6 $mM^{-1}s^{-}$, 203.9 $mM^{-1}s^{-1}$ and 202.1$mM^{-1}s^{-1}$ respectively.[54] The values represent that r_2 is based on the composition of the nanocrystals. Since MnIOs shows higher r_2 value compared to iron oxide alone, even with the lower saturation magnetization. This suggests that the relaxivity coefficient is not only dependent on the magnetic saturation of the nanostructure but also its geometry.[55] Another possible explanation for faster relaxation of proton may be due to the higher magnetic moment of manganese ion in the crystals. Furthermore the presence of citrate molecule in the MnIOs surface retards the r_2 relaxivity. The increase of

coating thickness decreases the outer-sphere contribution of the core towards r_2 due to the distance of closest approach of diffusing bulk water molecules to the superparamagnetic core of the particle.[56] Also, the relatively smaller size of MnIO25 and MnIO50 nanoparticles have greater surface- to- volume ratio and a greater number of hydrogen nuclei of water in proximity as compared with MnIO75. Therefore, decrease in coating thickness result in increase of the diffusing bulk water molecules to the superparamagnetic core of the particle. It further plays a role on the r_2 relaxivity and rapidly decreases T_2 relaxation time or dephasing of the water proton.

3. Conclusion

In summary, the SPION and phase pure bivalent manganese ion substituted SPION with molar concentrations 25%, 50% and 75% of Fe^{2+} ion were successfully synthesized through an aqueous co-precipitation method. The nanoparticle stabilized with hydrophilic layer of TSC in an in situ technique led to the formation of small size particle with easy water dispersion. The incorporation of manganese ion changed the magnetic proprieties and significantly modified T_2 MRI contrast as compared with conventional Fe_3O_4. The MnIO25, MnIO50 and MnIO75 exhibited r_2 ralaxivities of 236.6, 203.9 and 202.1$mM^{-1}s^{-1}$ respectively at 1.5T, which demonstrates that the nanoparticles can function as an efficient T_2 contrast agent. Further, the preliminary cytotoxic test by alamar blue assay, hemolysis and blood cell aggregation studies reveals that the nanoparticles are non toxic. This validates a cost – effective route for the high yield formation of water dispersible MnIOs, with remarkable MRI contrast property, biocompatibility which can serve as potential candidate in biomedical applications.

4. Experimental section

$FeCl_2.4H_2O$ (≥99%), $FeCl_3$ anhydrous (≥98%), $MnCl_2.4H_2O$ (≥99%), NaOH, 35% HCl and TSC were purchased from Merck (Germany/India). The chemicals used for the cell culture studies are 3-[4,5- dimethylthiazol-2yl]-2,5-diphenyltetrazolium bromide (MTT), F12K medium, sodium bicarbonate, Gentamicin (Himedia, India), Amphotericin B solution and Foetal Bovine Serum (Sigma–Aldrich, Germany). The chemicals used for the nanoparticle cell uptake and blood compatibility evaluations are from Sigma–Aldrich, Germany. Deionized water was used for the synthesis and subsequent washing of MnIO. All reagents were used without further purification.

MnIO with varying Mn^{2+} molar concentrations were synthesized by aqueous co-precipitation method. Briefly, the precipitation was carried out in the precursor of 0.1M solution of ferric salt in deionized water and 0.05 M solution of ferrous and manganese salts in 1M HCl. Trisodium citrate of 0.03M was added to this solution for restricting the particle aggregation and controlling the crystal growth. This precursor was magnetically stirred at a temperature of 80°C in an inert atmosphere followed by drop wise by addition of 1M NaOH, monitoring the pH continuously. At a pH >12, a black precipitate was observed indicating the formation of MnIO. After completing the addition of NaOH solution, the reaction was allowed to continue for another 2h for completing the precipitation of stable MnIO. The black precipitate obtained was magnetically separated, washed initially with deionized water followed by washing with 0.001M HCl to get complete dispersion of nano crystals in aqueous solution. This was further washed with deionized water to attain neutral pH.

The experimental procedure was repeated for various molar compositions of Mn^{2+} to Fe^{2+} ratios of 1:3, 1:1 and 3:1 keeping the concentration of ferric salt solution constant, (represented as MnIO25, MnIO50and MnIO75 respectively). Bare SPIONs were prepared as

per previously reported procedure by containing ferrous and ferric chlorides in 1:2 ratios under the same reaction conditions.[45]

The size and morphology of the prepared nanoparticles were studied by transmission electron microscopy at 100 kV (TEM, JEM-2010, JEOL, Tokyo, Japan) and the histogram of TEM particles were evaluated using ImageJ software by counting 50 number and corresponding average particle sizes were calculated with the help of Gaussian fit. HRTEM images were obtained by means of a Hitachi HF 2200 TU field emission microscope operating at an accelerating voltage of 200kV. The nano crystal phase analysis was carried out by powder X-ray diffraction. The powder X-ray diffraction measurements were taken by X-ray diffractometer (Bruker, D8 advance, Karlsruhe, Germany) using the Cu$K_{\alpha 1}$ radiation operating at 40 kV and 30 mA current strength and performed at room temperature. FT-IR for all samples were recorded on a Thermo-Nicolet 5700 spectrometer (Thermo Nicolet 5700, USA) using the diffuse reflectance (DRIFT) mode and to obtain high signal to noise ratio, 64 scans were collected at a resolution of 4 cm^{-1}. Thermogravimetric analysis (TGA) was performed for freeze-dried MnIOs samples with a SDT 2960 V2.2B (Simultaneous TGA-DTA, TA Instruments, Delaware, USA) instrument under nitrogen atmosphere employing a heating rate of 10^{o}C/min. The total atomic percentage of iron and manganese were determined by inductively coupled plasma- optical emission spectroscopy (ICP-OES, Perkin Elmer 5300DV, USA)). Aliquot (typically 2mL) of MnIO nanoparticle dispersions with 1mL 3N analar grade HCl were used for ICP measurements. The sample solutions were pre-heated to boiling and cooled to room temperature, followed by adjusting the volume to 50 or 100mL as per required analysis conditions and measurements were conducted. An environmental scanning electron microscope (Quanta 200, The Netherlands) equipped with an energy dispersive X- ray (EDS) spectrum was used to determine the morphology and composition of the as-prepared MnIOs samples.

Magnetic measurements were done on PAR EG&G Model 4500 Vibrating sample magnetometer (VSM) by varying the field between -15 kOe and +15 kOe. Powder samples of MnIOs were placed in a uniform magnetic field and its magnetic property, saturation magnetization and magnetic hysteresis nature were studied at room temperature.

Relaxivity Measurements: To assess the magnetic characteristics of the nanoparticles with respect to their potential use as MRI contrast agents, MnIOs r_2 relaxivity (relaxation of transverse magnetization, *i.e* spin-spin interaction) was measured. The decay of the transverse relaxation can be characterized by the transverse relaxation time T_2, which is the time which the transverse magnetization has decayed to 37% (e^{-1}) of its initial value after spin excitation. The relaxation rate r_2 is defined as the inverse of the relaxation time ($r_2 = 1/T_2$).

The magnetic relaxivity measurements phantom study were performed on a 1.5T whole body MRI scanner (MAGNETOM Avento Tim, Siemens, Munich, Germany) using a 12 channel head coil. Different concentrations of the samples dispersed uniformly in DI water and enclosed in non magnetic containers served as the phantoms. The relaxation times T_2 of different concentrations of nanoparticles (0 to 0.25 mM) were measured. The concentrations of nanoparticles were calculated with the help of ICP-OES analysis. From the stock concentration of MnIOs, different dilutions were made using DI water. The ionic concentration of each dilution was assessed via ICP-OES analysis. The scanning parameters used were, temperature = 22^{o}C, field of view = 20cm × 40cm and slice thickness = 6mm. For T_2 relaxometric measurements, spin echo sequence from three different planes of the phantoms was used.The MR signal was measured for varying echo times of 15-120ms with a fixed repetition time of 2000ms. T_2 relaxation time was calculated from the resulting MRI pixel intensity maps with respect to each concentration. The relaxivity (r_2) value calculated via pixel intensity plotted against the MnIO concentrations and r_2 value was determined by the linear fit.

$$1/T'_2=1/T_2+r_2*c \quad [57]$$

Where T_2 refers to the intrinsic T_2 time of the sample, T'_2 is the reduced T_2 time resulting from the contrast agent, r_2 is the transverse relaxivity of the contrast agent, and c is the concentration of the contrast-agent.

Acknowledgment

Authors express sincere thanks to Director, Head BMT Wing, SCTIMST for facilities. Acknowledge funding from DST, Govt. of India, for the financial support under 'Synthesis of oxide based magnetic nanoparticles for biocompatibility studies, magnetic hyperthermia and MRI application program. We thank Dr. Lissy KK and Mr. Ranjith S SCTIMST Trivandrum, Dr. Manoj Rama Varma NIIST Trivardrum & Dr, Sathikumar Toyo University, Japan for help with analysis facilities.

References

1 M. Mahmoudi, H. Hosseinkhani, M. Hosseinkhani, S. Boutry, A. Simchi, W. S. Journeay, K. Subramani and S. Laurent, *Chem. Rev.*, 2011, **111**, 253–280.

2 U. Jeong, X. Teng, Y. Wang, H. Yang and Y. Xia, *Adv. Mater.*, 2007, **19**, 33–60.

3 N. K. Verma, K. Crosbie-Staunton, A. Satti, S. Gallagher, K. B. Ryan, T. Doody, C. McAtamney, R. MacLoughlin, P. Galvin, C. S. Burke, Y. Volkov and Y. K. Gun'ko, *J. Nanobiotechnology*, 2013, **11**, 1.

4 M. Guo, C. Que, C. Wang, X. Liu, H. Yan and K. Liu, *Biomaterials*, 2011, **32**, 185–194.

5 M. Creixell, A. C. Bohórquez, M. Torres-Lugo and C. Rinaldi, *ACS Nano*, 2011, **5**, 7124–7129.

6 A. Kaushik, R. Khan, P. R. Solanki, P. Pandey, J. Alam, S. Ahmad and B. D. Malhotra, *Biosens. Bioelectron.*, 2008, **24**, 676–683.

7 A. Ali, M. S. AlSalhi, M. Atif, A. A. Ansari, M. Q. Israr, J. R. Sadaf, E. Ahmed, O. Nur and M. Willander, *J. Phys. Conf. Ser.*, 2013, **414**, 012024.

8 H. B. Na, I. C. Song and T. Hyeon, *Adv. Mater.*, 2009, **21**, 2133–2148.

9 J.-H. Lee, Y.-M. Huh, Y. Jun, J. Seo, J. Jang, H.-T. Song, S. Kim, E.-J. Cho, H.-G. Yoon, J.-S. Suh and J. Cheon, *Nat. Med.*, 2007, **13**, 95–99.

10 D. Carta, M. F. Casula, A. Falqui, D. Loche, G. Mountjoy, C. Sangregorio and A. Corrias, *J. Phys. Chem. C*, 2009, **113**, 8606–8615.

11 J. Lu, S. Ma, J. Sun, C. Xia, C. Liu, Z. Wang, X. Zhao, F. Gao, Q. Gong, B. Song, X. Shuai, H. Ai and Z. Gu, *Biomaterials*, 2009, **30**, 2919–2928.

12 J. Jang, H. Nah, J.-H. Lee, S. H. Moon, M. G. Kim and J. Cheon, *Angew. Chem. Int. Ed.*, 2009, **48**, 1234–1238.

13 A. R. West, *Basic solid state chemistry*, J. Wiley and sons, Chichester, 1988.

14 R. C. O'Handley, *Modern Magnetic Materials: Principles and Applications*, Wiley-Interscience, New York, 1 edition., 1999.

15 S. Sun, H. Zeng, D. B. Robinson, S. Raoux, P. M. Rice, S. X. Wang and G. Li, *J. Am. Chem. Soc.*, 2004, **126**, 273–279.

16 M. Stuber, W. D. Gilson, M. Schär, D. A. Kedziorek, L. V. Hofmann, S. Shah, E.-J. Vonken, J. W. M. Bulte and D. L. Kraitchman, *Magn. Reson. Med. Off. J. Soc. Magn. Reson. Med. Soc. Magn. Reson. Med.*, 2007, **58**, 1072–1077.

17 C. Bárcena, A. K. Sra, G. S. Chaubey, C. Khemtong, J. P. Liu and J. Gao, *Chem. Commun.*, 2008, 2224–2226.

18 F. Chen, W. Bu, C. Lu, G. Chen, M. Chen, X. Shen, R. Liu and J. Shi, *J. Nanosci. Nanotechnol.*, 2011, **11**, 10438–10443.

19 V. Mariani, J. Ponti, G. Giudetti, F. Broggi, P. Marmorato, S. Gioria, F. Franchini, H. Rauscher and F. Rossi, *Nanotoxicology*, 2012, **6**, 272–287.

20 L. Horev-Azaria, G. Baldi, D. Beno, D. Bonacchi, U. Golla-Schindler, J. C. Kirkpatrick, S. Kolle, R. Landsiedel, O. Maimon, P. N. Marche, J. Ponti, R. Romano, F. Rossi, D. Sommer, C. Uboldi, R. E. Unger, C. Villiers and R. Korenstein, *Part. Fibre Toxicol.*, 2013, **10**, 32.

21 Y. Anzai, C. W. Piccoli, E. K. Outwater, W. Stanford, D. A. Bluemke, P. Nurenberg, S. Saini, K. R. Maravilla, D. E. Feldman, U. P. Schmiedl, J. A. Brunberg, I. R. Francis, S. E. Harms, P. M. Som, C. M. Tempany and Group, *Radiology*, 2003, **228**, 777–788.

22 C. C. Berry, S. Charles, S. Wells, M. J. Dalby and A. S. G. Curtis, *Int. J. Pharm.*, 2004, **269**, 211–225.

23 P. L. Apopa, Y. Qian, R. Shao, N. L. Guo, D. Schwegler-Berry, M. Pacurari, D. Porter, X. Shi, V. Vallyathan, V. Castranova and D. C. Flynn, *Part. Fibre Toxicol.*, 2009, **6**, 1.

24 J. M. Veranth, E. G. Kaser, M. M. Veranth, M. Koch and G. S. Yost, *Part. Fibre Toxicol.*, 2007, **4**, 2.

25 U. O. Häfeli, J. S. Riffle, L. Harris-Shekhawat, A. Carmichael-Baranauskas, F. Mark, J. P. Dailey and D. Bardenstein, *Mol. Pharm.*, 2009, **6**, 1417–1428.

26 A. Stroh, C. Zimmer, C. Gutzeit, M. Jakstadt, F. Marschinke, T. Jung, H. Pilgrimm and T. Grune, *Free Radic. Biol. Med.*, 2004, **36**, 976–984.

27 D. Carta, M. F. Casula, P. Floris, A. Falqui, G. Mountjoy, A. Boni, C. Sangregorio and A. Corrias, *Phys. Chem. Chem. Phys.*, 2010, **12**, 5074–5083.

28 Z. Li, S. X. Wang, Q. Sun, H. L. Zhao, H. Lei, M. B. Lan, Z. X. Cheng, X. L. Wang, S. X. Dou and G. Q. (Max) Lu, *Adv. Healthc. Mater.*, 2013, **2**, 958–964.

29 A.-H. Lu, E. L. Salabas and F. Schüth, *Angew. Chem. Int. Ed.*, 2007, **46**, 1222–1244.

30 P. P. Goswami, H. A. Choudhury, S. Chakma and V. S. Moholkar, *Ind. Eng. Chem. Res.*, 2013, **52**, 17848–17855.

31 U. I. Tromsdorf, N. C. Bigall, M. G. Kaul, O. T. Bruns, M. S. Nikolic, B. Mollwitz, R. A. Sperling, R. Reimer, H. Hohenberg, W. J. Parak, S. Förster, U. Beisiegel, G. Adam and H. Weller, *Nano Lett.*, 2007, **7**, 2422–2427.

32 Z. Li, P. W. Yi, Q. Sun, H. Lei, H. Li Zhao, Z. H. Zhu, S. C. Smith, M. B. Lan and G. Q. (Max) Lu, *Adv. Funct. Mater.*, 2012, **22**, 2387–2393.

33 Z. Li, B. Tan, M. Allix, A. I. Cooper and M. J. Rosseinsky, *Small*, 2008, **4**, 231–239.

34 J.-H. Lee, Y.-M. Huh, Y. Jun, J. Seo, J. Jang, H.-T. Song, S. Kim, E.-J. Cho, H.-G. Yoon, J.-S. Suh and J. Cheon, *Nat. Med.*, 2007, **13**, 95–99.

35 R. A. Sperling and W. J. Parak, *Philos. Trans. R. Soc. Math. Phys. Eng. Sci.*, 2010, **368**, 1333–1383.

36 E. Dubois, V. Cabuil, F. Boué and R. Perzynski, *J. Chem. Phys.*, 1999, **111**, 7147–7160.

37 Y. F. Shen, J. Tang, Z. H. Nie, Y. D. Wang, Y. Ren and L. Zuo, *Sep. Purif. Technol.*, 2009, **68**, 312–319.

38 C. Pereira, A. M. Pereira, C. Fernandes, M. Rocha, R. Mendes, M. P. Fernández-García, A. Guedes, P. B. Tavares, J.-M. Grenèche, J. P. Araújo and C. Freire, *Chem. Mater.*, 2012, **24**, 1496–1504.

39 S. L. Easo and P. V. Mohanan, *Carbohydr. Polym.*, 2013, **92**, 726–732.

40 M. Ma, Y. Zhang, W. Yu, H. Shen, H. Zhang and N. Gu, *Colloids Surf. Physicochem. Eng. Asp.*, 2003, **212**, 219–226.

41 M. J. B. M. Rêgo, S. M. Almeida, S. A. Bezerra, C. Júnior, L. B, E. I. C. Beltrão, M. J. B. M. Rêgo, S. M. Almeida, S. A. Bezerra, C. Júnior, L. B and E. I. C. Beltrão, *An. Acad. Bras. Ciênc.*, 2014, **86**, 1351–1358.

42 V. Yathindranath, L. Rebbouh, D. F. Moore, D. W. Miller, J. van Lierop and T. Hegmann, *Adv. Funct. Mater.*, 2011, **21**, 1457–1464.

43 T. J. Daou, J. M. Grenèche, G. Pourroy, S. Buathong, A. Derory, C. Ulhaq-Bouillet, B. Donnio, D. Guillon and S. Begin-Colin, *Chem. Mater.*, 2008, **20**, 5869–5875.

44 A. G. Roca, J. F. Marco, M. del P. Morales and C. J. Serna, *J. Phys. Chem. C*, 2007, **111**, 18577–18584.

45 R. S. Jayasree, V. U. Nayar and V. Jordanovska, *Spectrochim. Acta. A. Mol. Biomol. Spectrosc.*, 2006, **65**, 278–284.

46 S. Srivastava, R. Awasthi, N. S. Gajbhiye, V. Agarwal, A. Singh, A. Yadav and R. K. Gupta, *J. Colloid Interface Sci.*, 2011, **359**, 104–111.

47 S. S. Pati, S. Gopinath, G. Panneerselvam, M. P. Antony and J. Philip, *J. Appl. Phys.*, 2012, **112**, 054320.

48 A. Srivastava, V. G. Gunjikar and A. P. B. Sinha, *Thermochim. Acta*, 1987, **117**, 201–217.

49 M. Muruganandham, R. Amutha, B. Ahmmad, E. Repo and M. Sillanpää, *J. Phys. Chem. C*, 2010, **114**, 22493–22501.

50 H. Demiroğlu, *Blood*, 1997, **89**, 4236–4236.

51 A. J. Rondinone, C. Liu and Z. J. Zhang, *J. Phys. Chem. B*, 2001, **105**, 7967–7971.

52 B. H. Kim, N. Lee, H. Kim, K. An, Y. I. Park, Y. Choi, K. Shin, Y. Lee, S. G. Kwon, H. B. Na, J.-G. Park, T.-Y. Ahn, Y.-W. Kim, W. K. Moon, S. H. Choi and T. Hyeon, *J. Am. Chem. Soc.*, 2011, **133**, 12624–12631.

53 R. A. McCurrie, *Ferromagnetic Materials: Structure and Properties*, Academic, 1994.

54 A. Saraswathy, S. S. Nazeer, M. Jeevan, N. Nimi, S. Arumugam, V. S. Harikrishnan, P. R. H. Varma and R. S. Jayasree, *Colloids Surf. B Biointerfaces*, 2014, **117C**, 216–224.

55 A. F. Rebolledo, S. Laurent, M. Calero, A. Villanueva, M. Knobel, J. F. Marco and P. Tartaj, *ACS Nano*, 2010, **4**, 2095–2103.

56 S. L. C. Pinho, G. A. Pereira, P. Voisin, J. Kassem, V. Bouchaud, L. Etienne, J. A. Peters, L. Carlos, S. Mornet, C. F. G. C. Geraldes, J. Rocha and M.-H. Delville, *ACS Nano*, 2010, **4**, 5339–5349.

57 J. Wan, X. Jiang, H. Li and K. Chen, *J. Mater. Chem.*, 2012, **22**, 13500–13505.